Electronic Supplementary Material (ESI) for Journal of Materials Chemistry A.
This journal is © The Royal Society of Chemistry 2023

Support Information

Double-Shelled Zn-Co Single-Atoms Enable Enhanced Conversion Kinetics in Lithium–Sulfur Batteries

Jiafeng Wu[1], Yuanyi Feng[1], Yang Chen, Ting Fan[*] and Yingwei Li[*]

Key Laboratory of Fuel Cell Technology of Guangdong Province, School of Chemistry and Chemical Engineering, South China University of Technology, Guangzhou 510640, China.

Experimental Section

Preparation of Zn-Co-ZIF-8 and ZIF-8 nanocubes

In brief, 1.132 g of $Zn(NO_3)_2 \cdot 6H_2O$ and 0.0584 g of $Co(NO_3)_2 \cdot 6H_2O$ was added into 100 mL aqueous solution containing 0.016 g of cetyltrimethylammonium bromide (CTAB), marked as solution A. Meanwhile, 18.16 g of 2-methylimidazole (2-MeIm) was added into 100 mL of deionized water, marked as solution B. Afterward, the solution B was mixed with solution A under vigorous stirring and the mixed solution was placed without disturbance for 2 h. After centrifugation and washing, the obtained powders were dried overnight at 60 °C to yield Zn-Co-ZIF nanocubes. The preparation of ZIF-8 nanocubes used the same procedure while without using $Co(NO_3)_2 \cdot 6H_2O$.

Preparation of yolk-shell Zn-Co-ZIF-8 and ZIF-8 nanocubes

Typically, 50 mL of ethanol was mixed with a 50 mL aqueous solution containing 100 mg of tannic acid (TA). Then, Zn-Co-ZIF nanocubes were dispersed into the above solution under ultrasonic treatment. After stirring for 10 min, double-shelled Zn-Co-ZIF nanocubes were collected by centrifuging and washing. The preparation of yolk-shell ZIF-8 used the same procedure with ZIF-8 nanocubes as precursor.

Preparation of doubled-shelled Co SA@DNC, Zn SA@DNC and Zn-Co SA@DNC

Doubled-shelled Zn-Co SA@DNC and Co SA@DNC were obtained by carbonizing the as-obtained yolk-shell Zn-Co-ZIF-8 nanocubes at 700 and 1000 °C for 2 h under flowing Ar atmosphere with a ramping rate of 5 °C min^{-1}, respectively. The preparation of doubled-shelled Zn SA@DNC used the same procedure except for using yolk-shell ZIF-8 nanocubes as precursor.

Synthesis of the Zn SA@DNC/S, Co SA@DNC/S and Zn-Co SA@DNC/S

Sulfur was loaded onto Zn-Co SA@DNC by means of a typical melt diffusion process. Specifically, the host material Zn-Co SA@DNC was mixed with sulfur powder (3:7, weight ratio). Subsequently, the mixture was heated at 155 °C for 12 h under Ar atmosphere. The Zn SA@DNC/S and Co SA@DNC/S materials were obtained by using the identical process.

Materials characterization

The morphology and element distribution of samples were characterized by field-emission scanning electron microscope (SEM, HITACHI SU8220) and high-resolution transmission electron microscope (TEM, JEOL JEM-2100F). The crystal structures of the samples were collected on a Rigaku diffractometer (D/MAX-IIIA, 3 kW) using Cu Kα radiation (40 kV, 30 mA, λ = 0.1543 nm). X-ray photoelectron spectroscopy was obtained on a Kratos AxisUltra DLD system. High-angle annular dark-field scanning transmission electron microscopy (HAADF-STEM) was recorded using a Titan Cubed Themis G2300 (FEI, Netherlands) transmission electron microscope operated at 200 kV equipped with double spherical aberration correctors. The specific surface areas and pore size distributions of the samples were measured on a Micromeritics ASAP 2020 M instrument. TGA was carried out on a TA instrument of Q500 with a heating rate of 10 °C min^{-1} under N_2 atmosphere. The metal contents of the samples were determined by inductively coupled plasma optical emission spectroscopy (ICP-OES) on an Optima 8300 instrument. The C and N elemental contents of the samples were measured on a Euro Vector EA3000 instrument.

X-ray absorption spectra (XAS) including X-ray absorption near-edge structure (XANES) and extended X-ray absorption fine structure (EXAFS) of the samples at Fe K-edge were collected at the Shanghai Synchrotron Light Source (SSLS) center, where a pair of channel-cut Si (111) crystals were used in the monochromator. Fe foil and Fe_3O_4 were used as references. The storage ring was working at the energy of 2.5 GeV with an average electron current of below 200 mA. The acquired EXAFS data were extracted and processed according to the standard procedures using the ATHENA module implemented in the IFEFFIT software packages.

Electrochemical characterization

The active materials (Zn SA@DNC/S, Co SA@DNC/S and Zn-Co SA@DNC/S), PVDF and Super P were mixed with a mass ratio of 8:1:1 in NMP. The prepared homogeneous slurry was coated on an aluminum foil and dried under vacuum at 60 °C overnight. The aluminum foil was then punched into disks with a diameter of 12 mm. The sulfur mass loading of cathode was 1.5 mg cm^{-2}. Electrodes with a high sulfur loading were also prepared. CR2025-type coin cells were assembled in an Ar-filled

glove box with Celgard 2400 membranes as separators and lithium metal as the counter electrode. The electrolyte consisted of 1.0 M LiTFSI in DOL and DME (v:v = 1:1) with 1 wt% $LiNO_3$. The electrolyte/sulfur ratio was typically 20 μL mg^{-1}. The cycling performance test was performed on a LAND CT2001A test system with the voltage window of 1.7 to 2.8 V. CV curves and EIS were recorded on an electrochemical workstation (CHI 760E).

Lithium polysulfide adsorption test

Mixing Li_2S and S (molar ratio/1:5) into DOL/DME (volume ratio/1:1) under vigorous stirring for 24 h at 50 °C was utilized to prepare the Li_2S_6 solution. To test the lithium polysulfides adsorption, the same mass of Zn SA@DNC, Co SA@DNC and Zn-Co SA@DNC were immersed into 5 mM Li_2S_6 solution, respectively. Then it was placed for 12 h to compare the polysulfide adsorption ability of Zn SA@DNC, Co SA@DNC and Zn-Co SA@DNC.

Assembly of symmetric cells and measurements

Two identical electrodes were utilized as working and counter electrodes with 40 μL of electrolyte containing 0.3 M Li_2S_6 and 1 M LiTFSI dissolved in DOL and DME (v:v = 1:1). For comparison, symmetric cell with 40 μL of electrolyte containing 1 M LiTFSI dissolved in DOL and DME (v:v = 1:1) was also assembled and tested. CV curves of the symmetrical cells were executed in the voltage ranging from −1.0 to 1.0 V. EIS was performed with the frequency range of 10^{-2} Hz to 10^{5} Hz and an amplitude of 10 mV.

Li_2S nucleation/decomposition measurements

The CR2025 coin cells were assembled with host materials (Zn SA@DNC, Co SA@DNC and Zn-Co SA@DNC) as work electrodes, and lithium foil as counter and reference electrode. 20 μL of Li_2S_8 electrolyte (0.3 M) was dropped onto the cathode side, and then 20 μL of the conventional electrolyte without Li_2S_6 was added onto the anode side. To test the nucleation of Li_2S, the fresh cells were discharged galvanostatically at 0.112 mA to 2.06 V and then discharged potentiostatically at 2.05 V until the current decreased to 10^{-2} mA. To test the decomposition of Li_2S, fresh cells were discharged at 0.112 mA to 1.70 V and then potentiostatically charged at 2.35 V until the current decreased to 10^{-2} mA.

Theoretical calculation details

All calculations were performed with density functional theory implemented in the VASPwith generalized gradient approximation.[1-4] The Perdew-Burke-Ernzerhof (PBE) exchange-correlation functional and the Projector augmented wave (PAW) pseudopotential were used.[5, 6] DFT-D3 method with Becke-Jonson dampling was used to describe van der Waals interactions. The plane wave with a cutoff energy of 460 eV was used. For all the calculations, the convergence criteria were set to be 1×10^{-5} eV for wave-function and 0.02 eV/Å for geometric optimization. To avoid interaction between periodic images in the c direction, the vacuum layer was set as 14 Å. The Brillouin zone was sampled with 1×1×1 Monkhorst-Pack grid k-points for geometric optimization.[7]

To model Zn-N_4, Co-N_4, and Zn-Co-N_8, a supercell of graphene containing 6×6 unit cells was used. For Zn-N_4 and Co-N_4, two carbon atoms on the graphene surface were removed, and the four surrounding unsaturated carbons were replaced by nitrogens, leading to a porphyrin-like coordination environment.[8, 9] Similarly, to fabricate Zn-Co-N_8, four carbon atoms were removed and the eight surrounding unsaturated carbons were replaced by nitrogens.[10, 11] For the calculations of the formation energies (E_f) of different substrates, E_f is defined by eq 1:

$$E_f = E_{substrate} - E_{metal} - E_{CN_x} \quad (1)$$

Here $E_{substrate}$, E_{metal} and E_{CNx} are the energy of the substrate, a single metal atom, and graphene slab with defect, respectively. With this definition, a more negative formation energy indicates that the metal atom more tightly bonds to the graphene. And the adsorption energy of Li_2S_n on different substrates is defined as eq 2:

$$E_{ads}(X) = E_{X*} - E_X - E_* \quad (2)$$

In which E_{X*}, E_X, and E_* are the energy of Li_2S_n-substrate complex, the energy of Li_2S_n in the gas phase and the energy of the substrate, respectively. A more negative value suggests a more favorable adsorption.

For the discharging process, we assumed that S_8 undergoes the following reduction and disproportionation reactions [12]:

$$S_8 + Li \xrightarrow{(3)} Li_2S_8 \xrightarrow{(4)} Li_2S_6 \xrightarrow{(5)} Li_2S_4 \xrightarrow{(6)} Li_2S_2 \xrightarrow{(7)} Li_2S$$

The corresponding reaction energies for these five steps were calculated from the equations (3-7), respectively:

$$E_{Li_2S_8{}^*} - E_{S_8{}^*} - 2 \times E_{Li} \quad (3)$$

$$E_{Li_2S_6{}^*} + \frac{1}{4} \times E_{S_8} - E_{Li_2S_8{}^*} \quad (4)$$

$$E_{Li_2S_4{}^*} + \frac{1}{4} \times E_{S_8} - E_{Li_2S_6{}^*} \quad (5)$$

$$E_{Li_2S_2{}^*} + \frac{1}{4} \times E_{S_8} - E_{Li_2S_4{}^*} \quad (6)$$

$$E_{Li_2S^*} + \frac{1}{8} \times E_{S_8} - E_{Li_2S_2{}^*} \quad (7)$$

Where E_{Li} is the energy of Li cubic cell per atom and E_{S8} is the gas-phase energy of S_8 molecule.

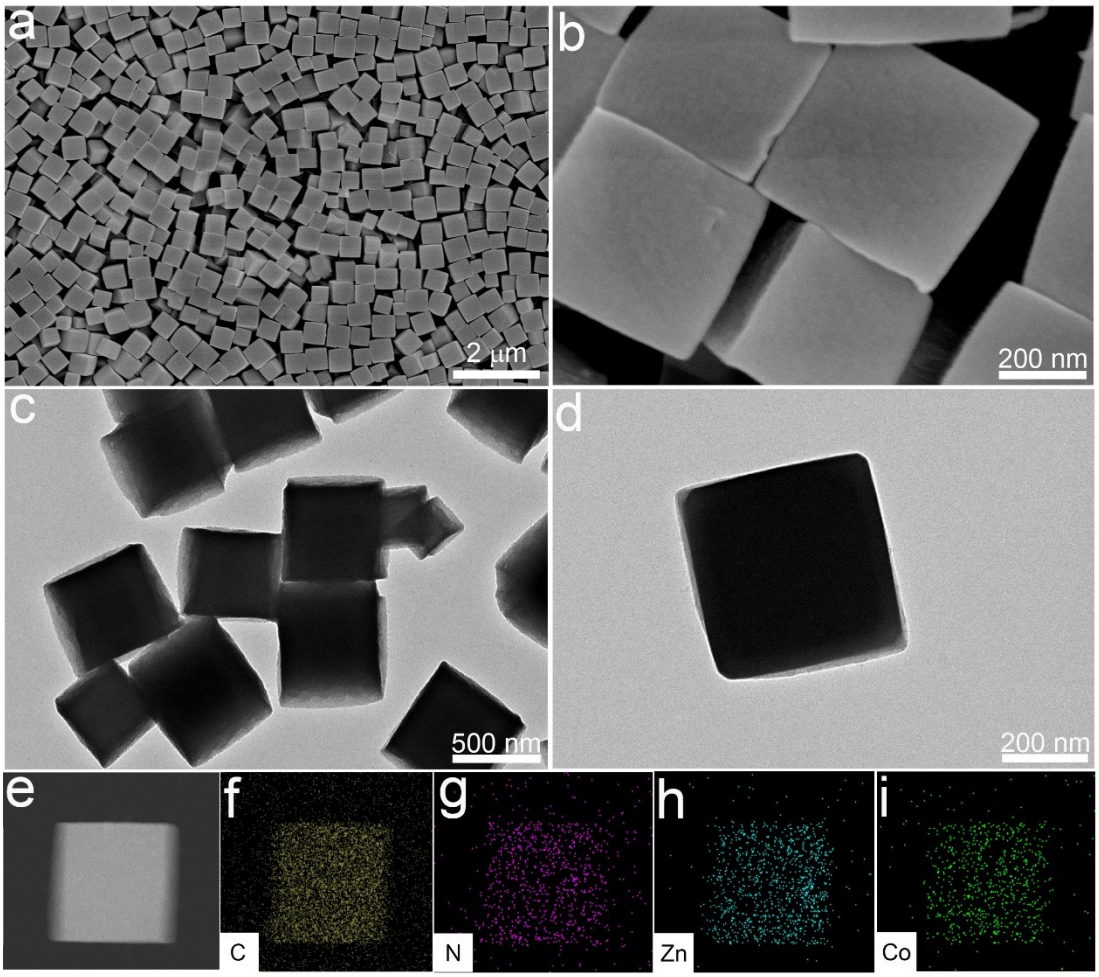

Fig. S1. (a, b) SEM, (c, d) TEM, (e) HAADF-STEM, and (f-i) corresponding elemental mappings of Zn-Co-ZIF-8 nanocubes.

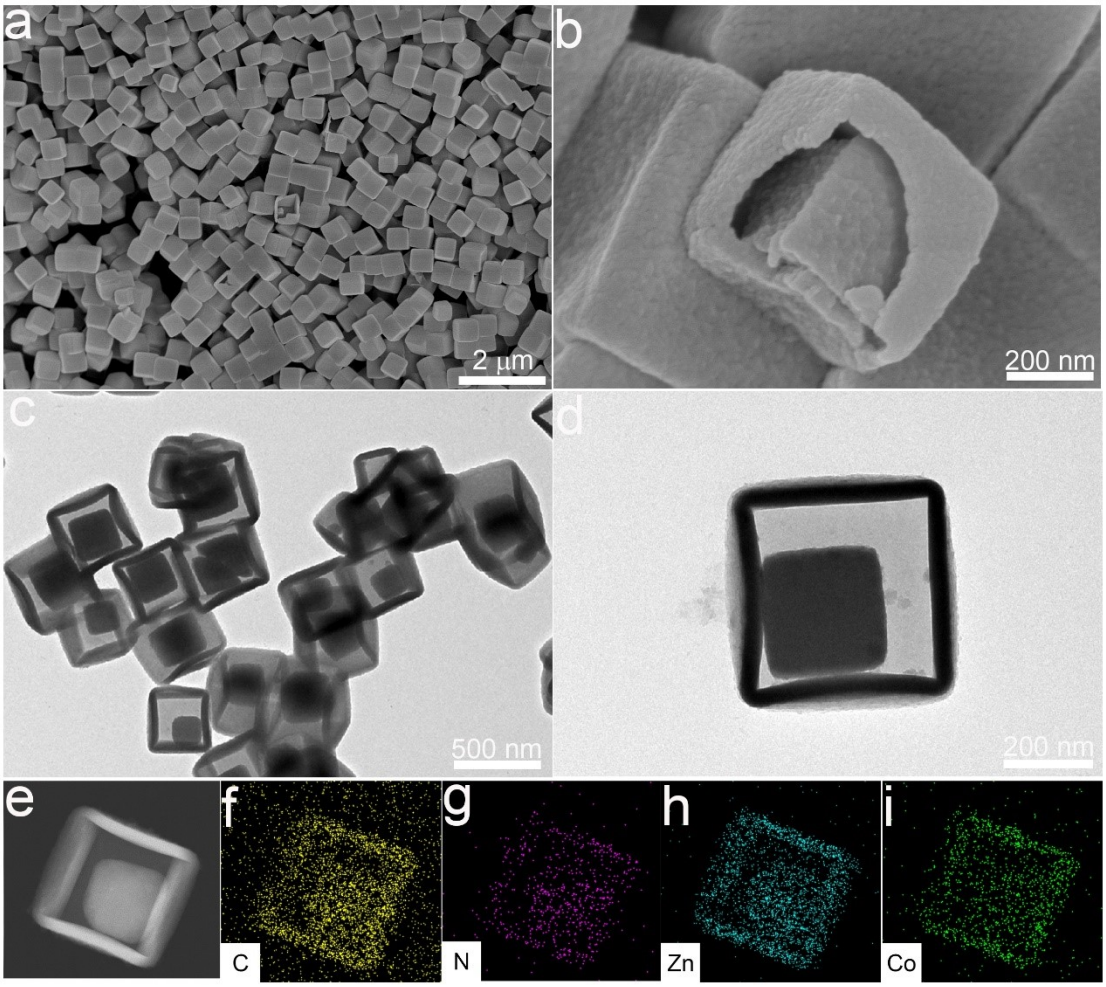

Fig. S2. (a, b) SEM, (c, d) TEM, (e) HAADF-STEM, and (f-i) corresponding elemental mappings of yolk-shell Zn-Co-ZIF-8 nanocubes.

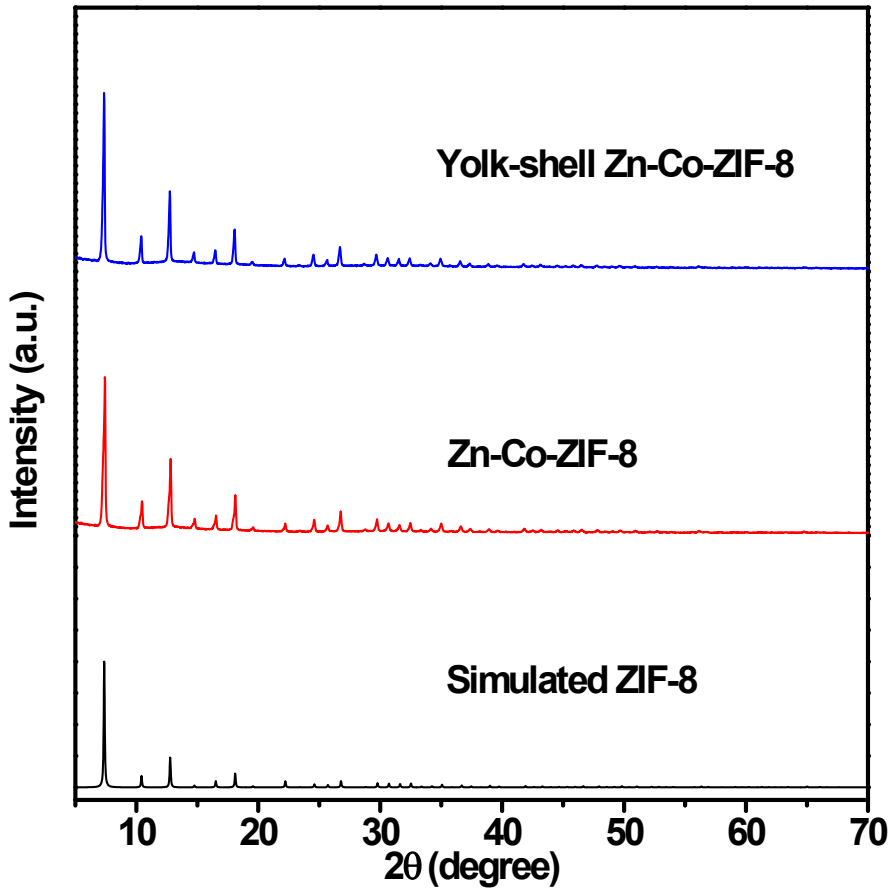

Fig. S3. XRD patterns of Zn-Co-ZIF-8 nanocubes and yolk-shell Zn-Co-ZIF-8 nanocubes.

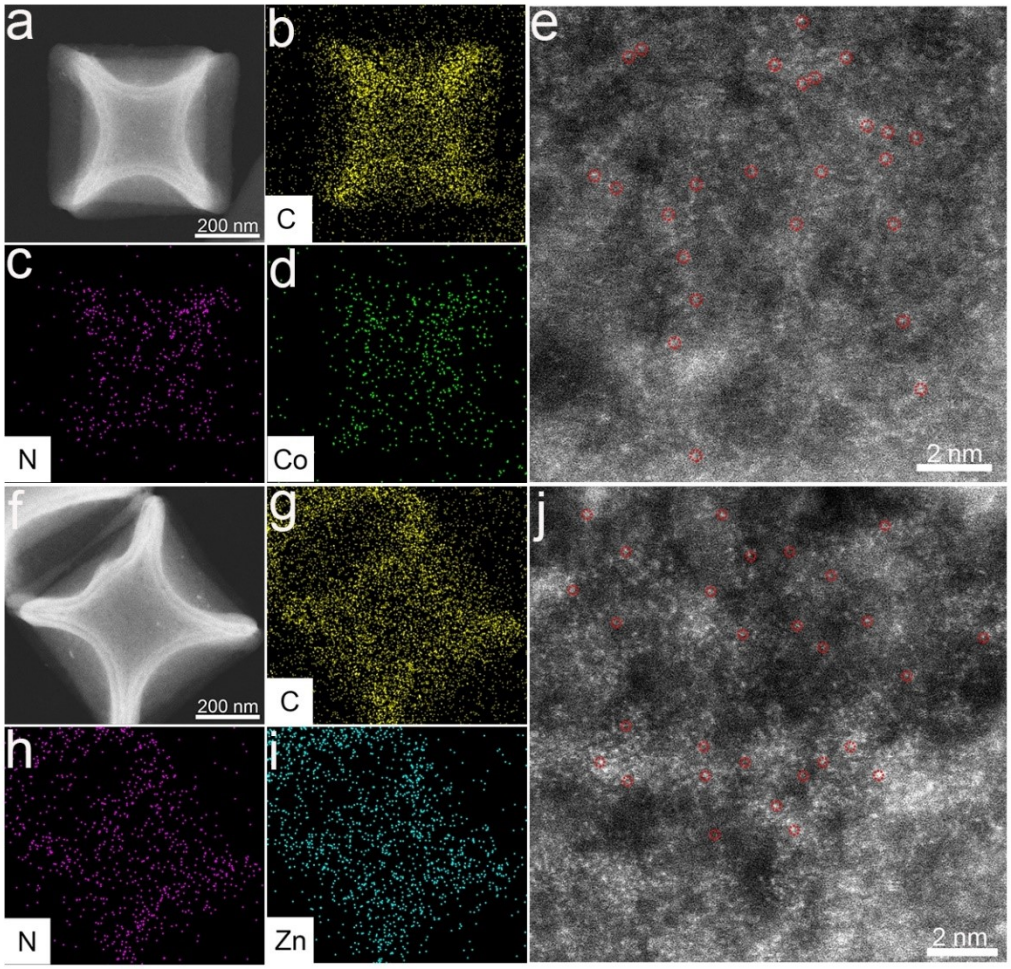

Fig. S4. (a, f) HAADF-STEM, (b-d, g-i) corresponding elemental mappings, and Aberration-corrected HAADF-STEM of Co SA@DNC (e) and Zn SA@DNC (j).

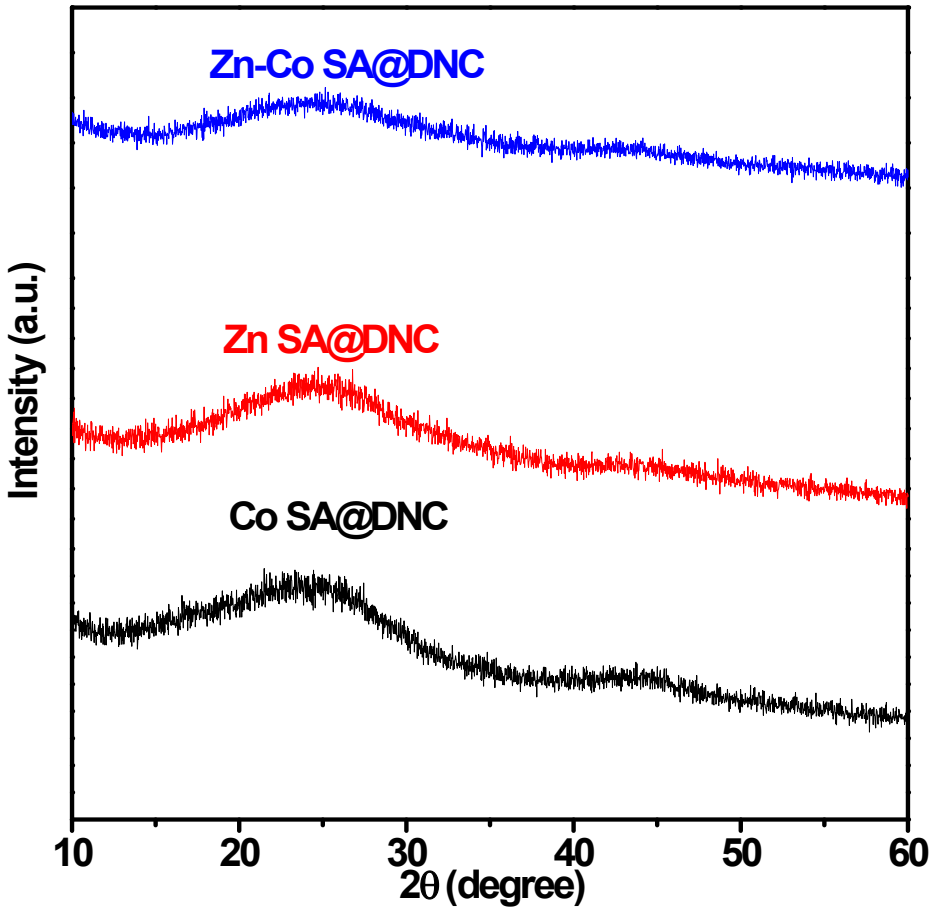

Fig. S5. XRD patterns of Co SA@DNC, Zn SA@DNC and Zn-Co SA@DNC.

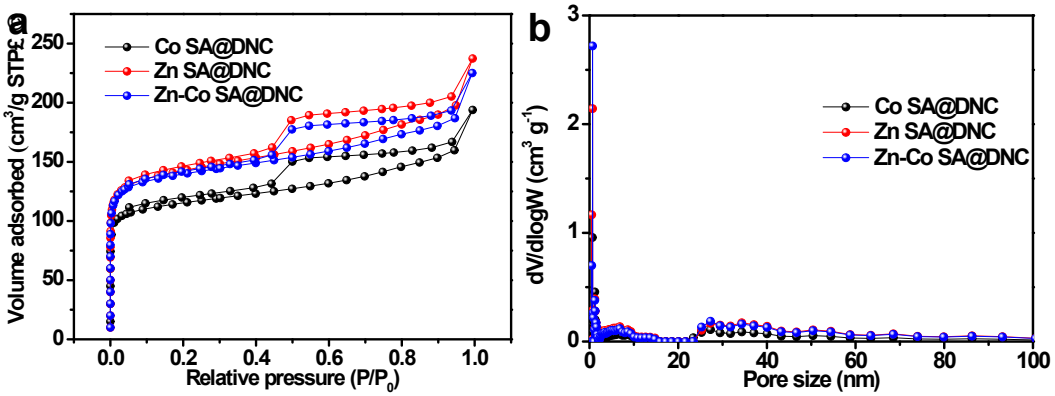

Fig. S6. (a) nitrogen adsorption-desorption isotherms, and (b) pore size distributions of Co SA@DNC, Zn SA@DNC and Zn-Co SA@DNC.

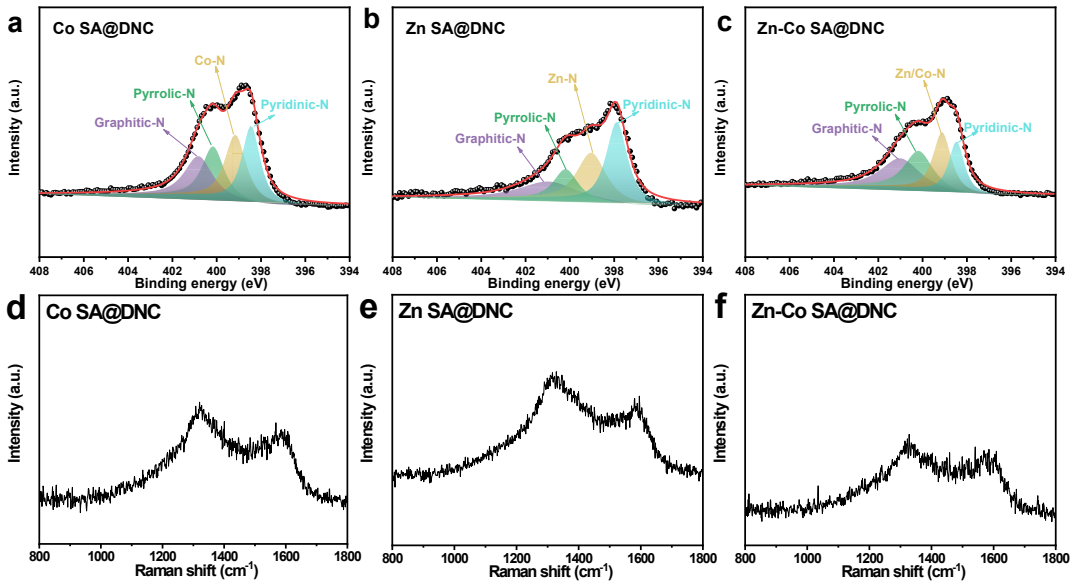

Fig. S7. (a-c) High-resolution N 1s XPS and (d-f) Raman spectra of Co SA@DNC, Zn SA@DNC and Zn-Co SA@DNC.

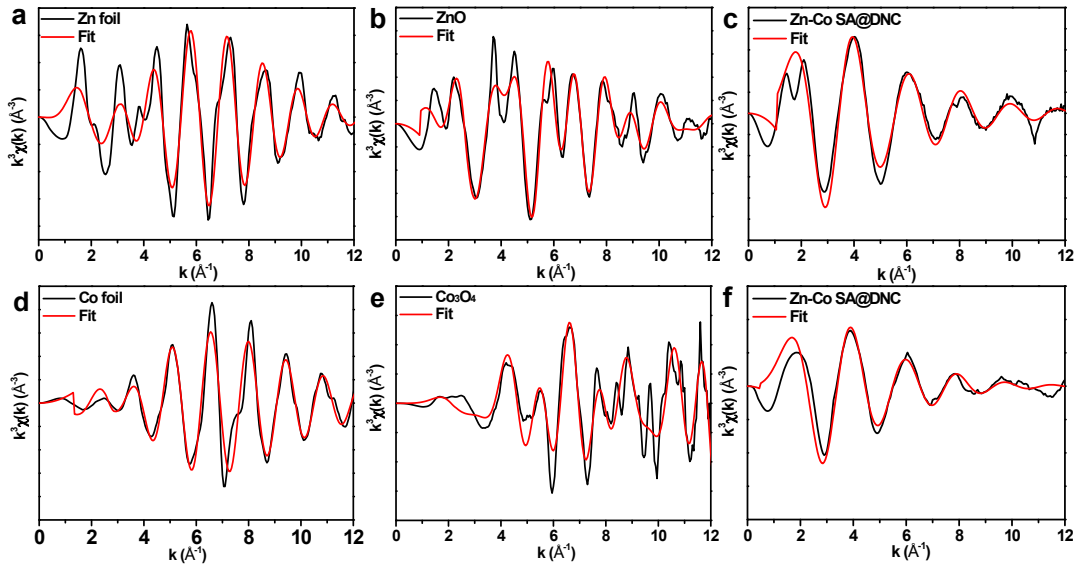

Fig. S8. Corresponding Zn K-edge EXAFS fitting curves of (a) Zn foil, (b) ZnO, and (c) Zn-Co SA@DNC. Corresponding Co K-edge EXAFS fitting curves of (d) Co foil, (e) Co_3O_4, and (f) Zn-Co SA@DNC.

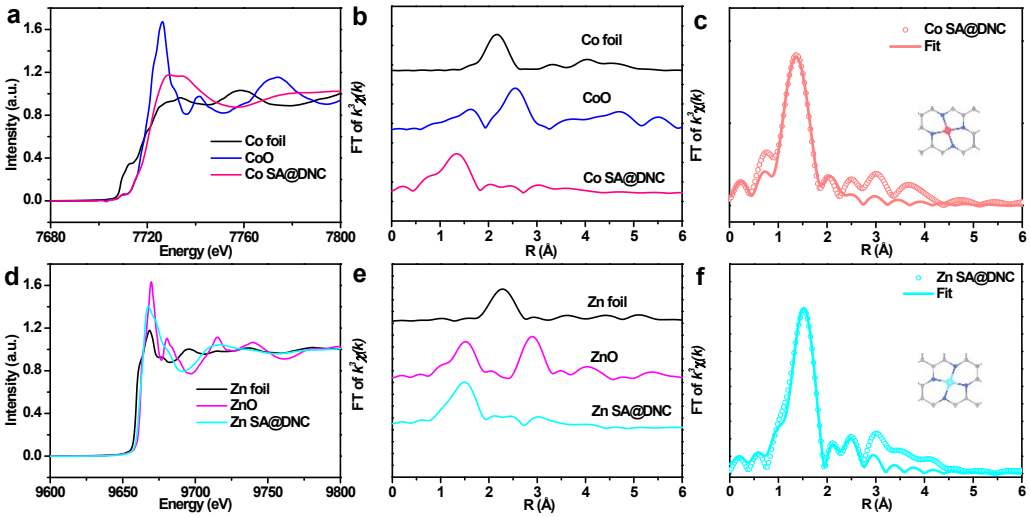

Fig. S9. (a) Co K-edge XANES spectra of Co SA@DNC, CoO and Co foil, (b) Fourier transforms k^3-weighted EXAFS spectra of Co SA@DNC, CoO and Co foil, (c) Co K-edge EXAFS fitting curves of Co SA@DNC in R space. (d) Zn K-edge XANES spectra of Zn SA@DNC, ZnO and Zn foil, (e) Fourier transforms k^3-weighted EXAFS spectra of Zn SA@DNC, ZnO and Zn foil, (f) Zn K-edge EXAFS fitting curves of Zn SA@DNC in R space.

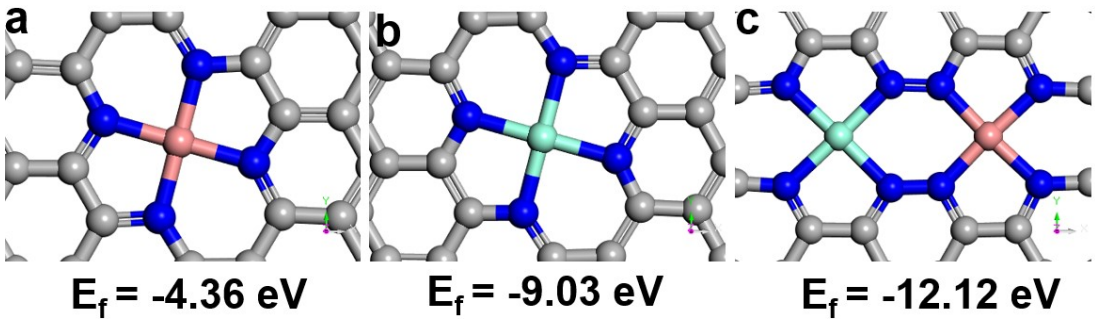

Fig. S10. Optimized geometrical configurations and corresponding formation energies of (a) Zn SA@DNC, (b) Co SA@DNC, and (c) Zn-Co SA@DNC. Zn, Co, C, and N atoms are in cyan, pink, grey, and blue, respectively.

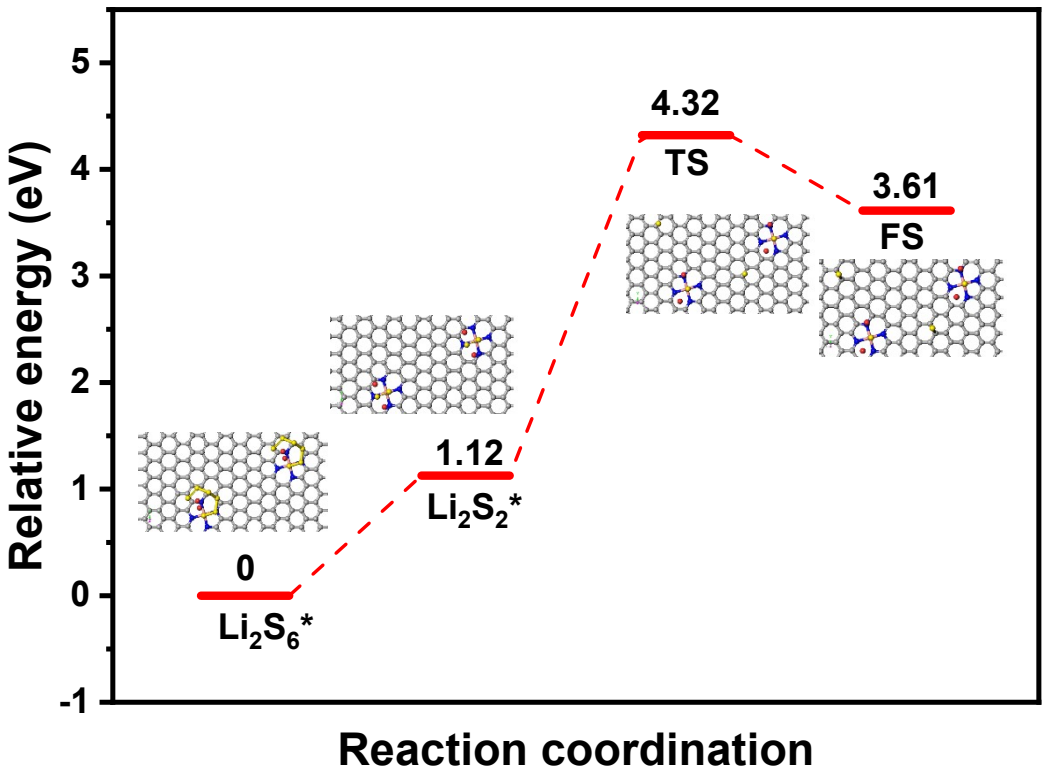

Fig. S11. Energy profiles of the decomposition of Li_2S_6 on Co SA@DNC. Co, C, N, S and Li atoms are in pink, grey, blue, yellow and red, respectively.

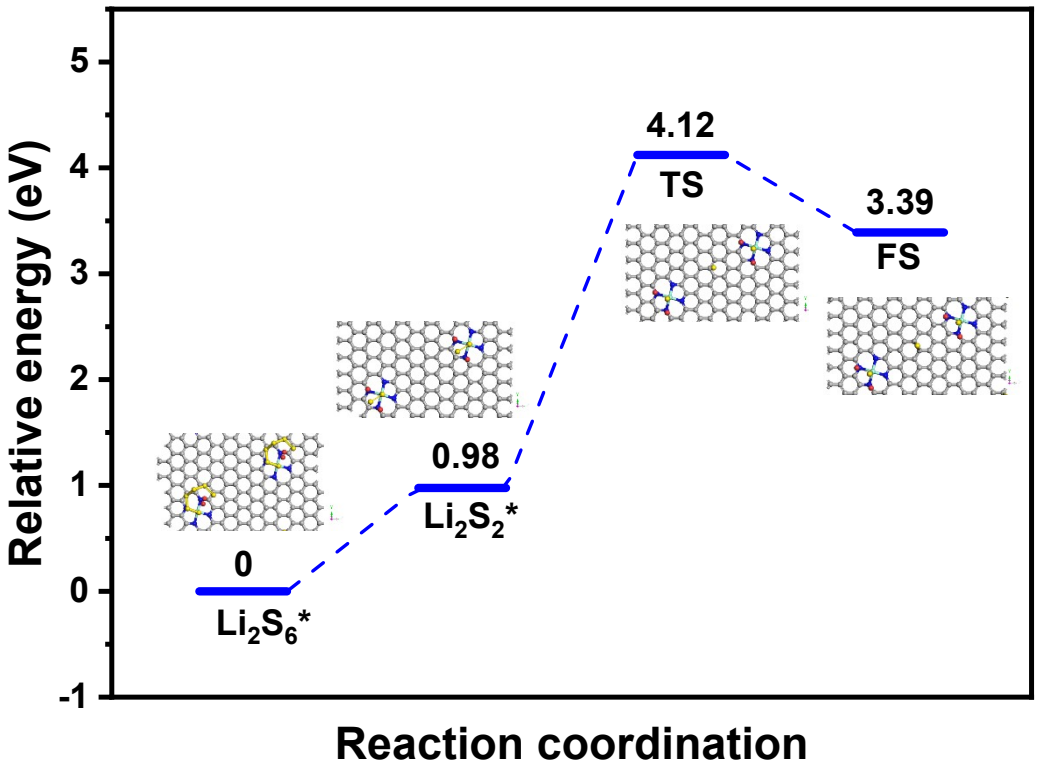

Fig. S12. Energy profiles of the decomposition of Li_2S_6 on Zn SA@DNC. Zn, C, N, S and Li atoms are in cyan, grey, blue, yellow and red, respectively.

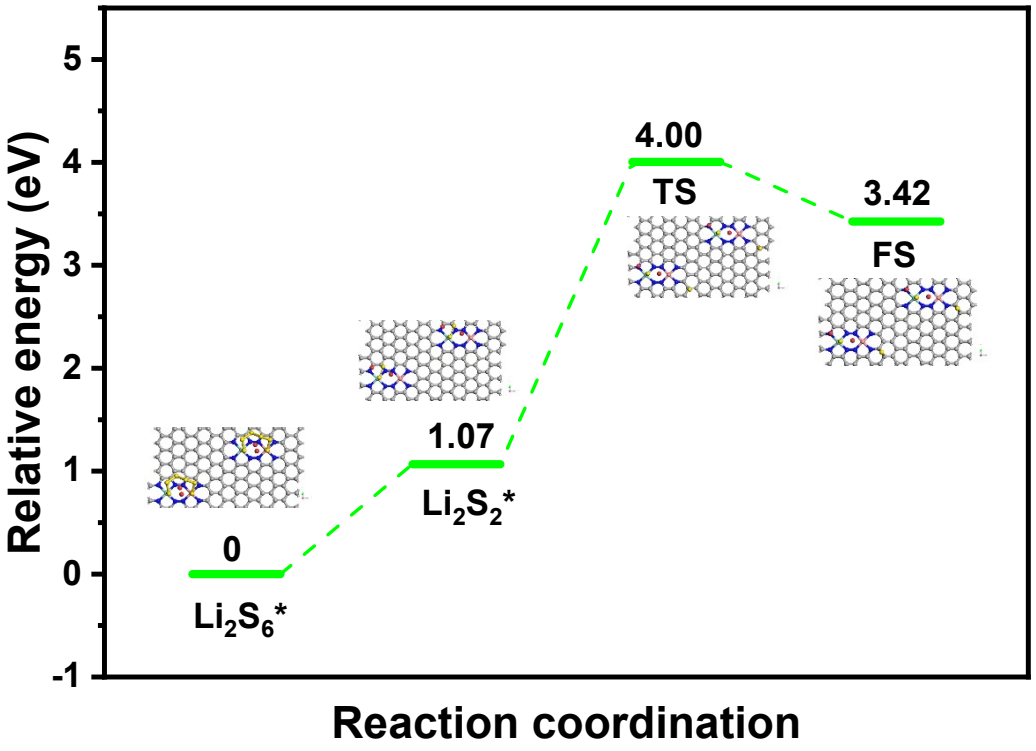

Fig. S13. Energy profiles of the decomposition of Li_2S_6 on Zn-Co SA@DNC. Zn, Co, C, N, S and Li atoms are in cyan, pink, grey, blue, yellow and red, respectively.

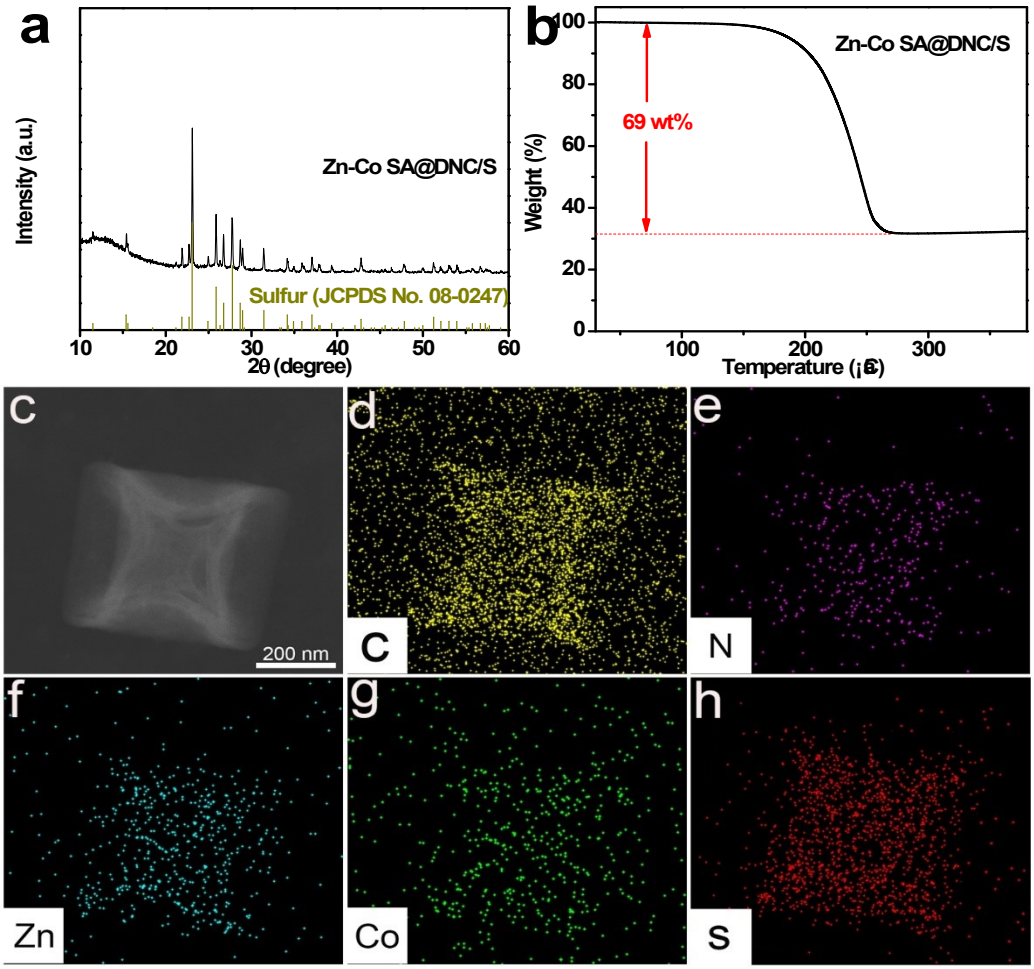

Fig. S14. (a) XRD pattern, (b) TGA curve, (c) TEM image and (d-h) elemental mappings of Zn-Co SA@DNC/S cathode.

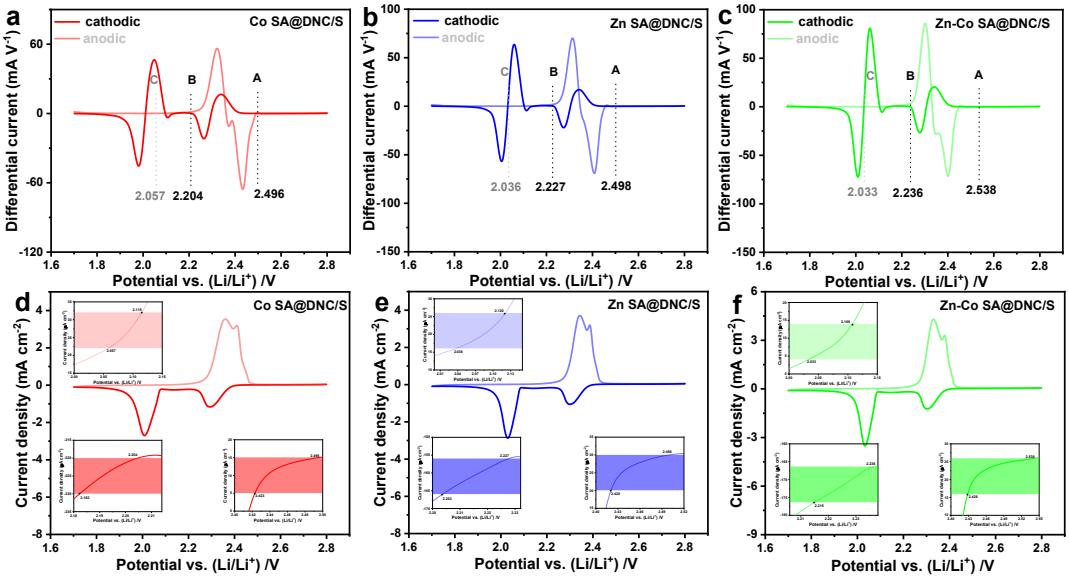

Fig. S15. Onset potential tests for LSBs redox reactions. Differential CV curves with (a, d) Co SA@DNC/S, (b, e) Zn SA@DNC/S, and (c, f) Zn-Co SA@DNC/S cathodes. The baseline voltage and current density are defined as the value before the redox peak, where the variation on current density is the smallest, namely $dI/dV = 0$. Baseline voltages are denoted in gray for cathodic peak A, B and in black for anodic peak C, respectively. The CV curves and corresponding onset current density is 10 μA cm^{-2} beyond the corresponding baseline current density (more specifically, 10 μA cm^{-2} more negative than baseline current density for the cathodic peaks or 10 μA cm^{-2} more positive than baseline current density for anodic peaks). As shown in the inset, the baseline voltages are exhibited, and colored region indicates the gap in current density (10 μA cm^{-2}).

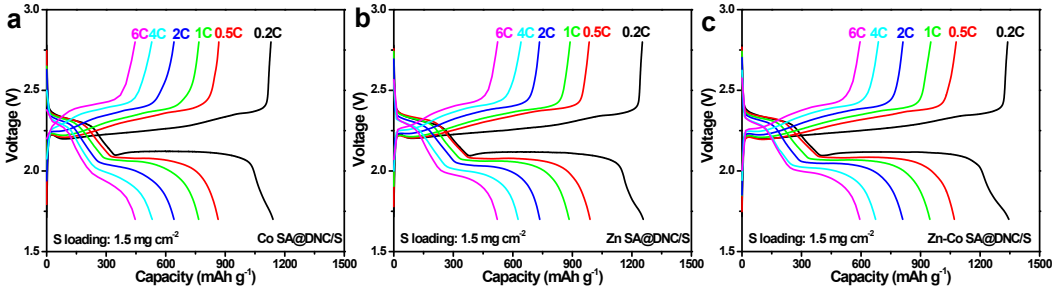

Fig. S16. The charge-discharge profiles of LSBs coupled with Co SA@DNC/S, Zn SA@DNC/S and Zn-Co SA@DNC/S under various current densities.

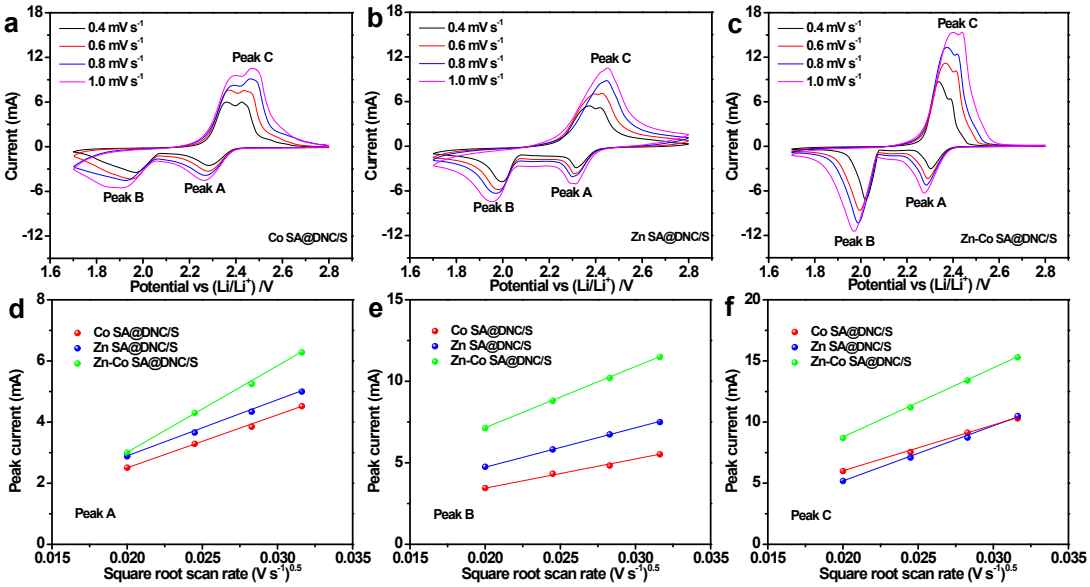

Fig. S17. CV curves of (a) Co SA@DNC/S, (b) Zn SA@DNC/S and (c) Zn-Co SA@DNC/S electrodes at various scan rates. Plots of CV peak current of (d) peak A, (e) peak B and (f) peak C vs. square root of the scan rates.

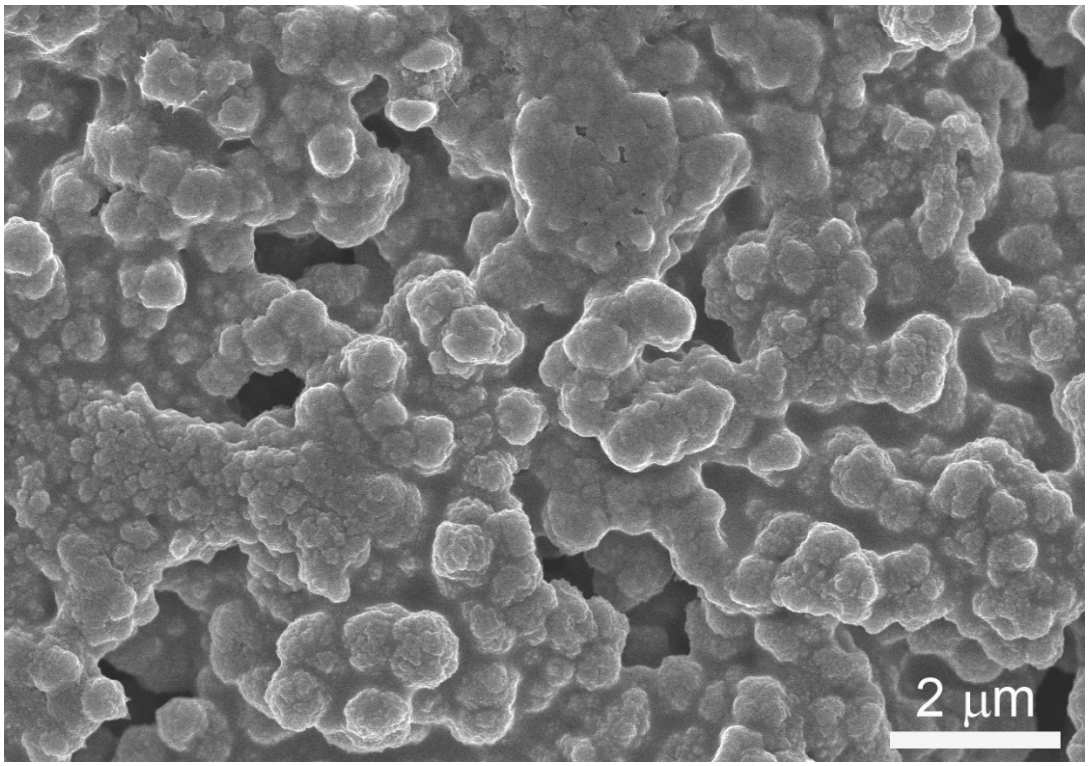

Fig. S18. SEM image of Zn-Co SA@DNC/S electrode after 800 cycles at 1 C.

Table S1. Elemental contents of the as-prepared SACs.

Sample	Mass contents (%)			
	C[a]	N[a]	Co[b]	Zn[b]
Co SA	79.6	14.1	1.2	-
Zn SA	66.5	20.0	-	7.2
Zn-Co SAs	67.3	20.4	1.0	5.1

[a] Measured by elemental analysis. [b] Measured by ICP-OES.

Table S2. Structural parameters of Zn-Co SA@DNC extracted from the EXAFS fitting (S_0^2=0.72, 0.76)

samples	path	C. N.[a]	R (Å) [b]	σ^2 ($\times 10^{-3}$ Å^2) [c]	ΔE (eV) [d]	R factor[e]
Zn foil	Zn-Zn	12*	2.64*	3.0±2.3	-2.5±2.3	0.01
ZnO	Zn-O	4*	1.98*	3.4±2.3	3.1±1.0	0.01
	Zn-O-Zn	6*	3.21*	18.6±2.5		
Zn-N-C	Zn-N	3.4±0.6	2.03±0.02	8.1±3.0	4.4±2.1	0.01
Co foil	Co-Co	12*	2.51*	6.1±0.2	6.5±0.3	0.01
Co_3O_4	Co-O	4*	1.96*	3.7±0.9	-9.4±4.2	0.03
	Co-O-Co	12*	3.34*	6.9±3.8		
	Co-O-Co	4*	3.49*	8.9±8.6		
Co-N-C	Co-N	3.4±0.6	2.08±0.02	2.9±1.8	0.8±2.3	0.01

[a] C. N.: coordination numbers; [b] *R*: bond distance; [c] σ^2: Debye-Waller factors; [d] ΔE_0: the inner potential correction. [e] *R* factor: goodness of fit. *The experimental EXAFS fit by fixing C. N. as the known crystallographic value.

Table S3. Structural parameters of Co SA@DNC extracted from the EXAFS fitting (S_0^2=0.95)

samples	path	C. N.[a]	R (Å) [b]	σ^2 ($\times 10^{-3}$ Å^2) [c]	ΔE (eV) [d]	R factor[e]
Co foil	Co-Co	12*	2.51*	6.6±0.8	6.3±1.8	0.01
CoO	Co-O	6*	2.13*	6.2±3.8	-3.1±1.6	0.01
	Co-O-Co	12*	3.01*	8.8±1.6		
Co-N-C	Co-N	3.7±1.5	2.02±0.02	6.7±5.6	-4.1±5.1	0.02

[a] C. N.: coordination numbers; [b] *R*: bond distance; [c] σ^2: Debye-Waller factors; [d] ΔE_0: the inner potential correction. [e] *R* factor: goodness of fit. *The experimental EXAFS fit by fixing C. N. as the known crystallographic value.

Table S4. Structural parameters of Zn SA@DNC extracted from the EXAFS fitting (S_0^2=0.76)

samples	path	C. N.[a]	R (Å) [b]	σ^2 ($\times 10^{-3}$ Å^2) [c]	ΔE (eV) [d]	R factor[e]
Zn foil	Zn-Zn	12*	2.64*	3.8±3.3	-2.1±1.8	0.01
ZnO	Zn-O	4*	1.98*	4.6±3.1	3.8±1.2	0.01
	Zn-O-Zn	6*	3.21*	9.8±6.1		
Zn-N-C	Zn-N	4.4±0.6	2.04±0.02	8.8±2.2	2.8±1.1	0.02

[a] C. N.: coordination numbers; [b] *R*: bond distance; [c] σ^2: Debye-Waller factors; [d] ΔE_0: the inner potential correction. [e] *R* factor: goodness of fit. *The experimental EXAFS fit by fixing C. N. as the known crystallographic value.

Table S5. Lithium-ion diffusion coefficient (D, cm^2 s^{-1}) of Co SA@DNC/S, Zn SA@DNC/S and Zn-Co SAs@DNC/S.

Sample	Peak A	Peak B	Peak C
Co SA@DNC/S	4.05×10^{-8}	4.28×10^{-8}	1.86×10^{-7}
Zn SA@DNC/S	4.48×10^{-8}	7.53×10^{-8}	2.83×10^{-7}
Zn-Co SA@DNC/S	1.08×10^{-7}	1.91×10^{-7}	4.36×10^{-7}

Table S6. Comparison of cycling performance of single-atom-based catalysts for LSBs.

Host material	Sulfur loading (mg cm^{-2})	Current density (C)	Initial capacity (mAh g^{-1})	Reversible capacity (mAh g^{-1})	Decay rate (per cycle, %)	cycle number	Ref
Zn-Co SA@DNC	1.5	1	1008	732	0.034	800	This work
ZnS/Co SA	1.2	1	~1060	~970	0.085	100	[12]
Co SA	2.0	1	927	681	0.053	500	[13]
Ni SA	1.3-1.6	0.5	1086	798	0.053	500	[14]
Ni SA	1.35-1.6	0.5	967	514	0.078	600	[15]
Fe_2N/Fe SA	1.5	0.2	936	801	0.029	500	[16]
Co SA	2.0	1	1059	737	0.051	600	[17]
Fe SA	1.3	0.1	1138	427	0.21	300	[18]
Mn SA	1.3	1	~900	450	0.05	1000	[19]
Fe SA	1.4-1.6	1	1052	790	0.12	200	[20]
Co SA	1.2	1	1061	675	0.35	1000	[21]
Fe/Co SA	2.1	1	977	658	0.11	300	[22]
Fe/Co SA	4.3	0.1	1034	981	0.087	60	[23]

References

1 G. Kresse, J. Furthmüller, Phys Rev B, 1996, **54**, 11169-11186.

2 G. Kresse, D. Joubert, , Phys Rev B, 1999, **59**,1758-1775.

3 G. Kresse, J. Furthmüller, Comput. Mater. Sci, 1996, **6**, 15-50.

4 G. Kresse, J. Hafner, J. Phys.: Condens. Matter, 1994, **6**, 8245.

5 J.P. Perdew, K. Burke, M. Ernzerhof, Phys. Rev. Lett., 1996, **77**, 3865-3868.

6 P.E. Blöchl, Phys Rev B, 1994, **50**, 17953-17979.

7 D. Vanderbilt, Phys Rev B, 1990, **41**, 7892-7895.

8 T. Kropp, M. Mavrikakis, ACS Catal., 2019, **9**, 6864-6868.

9 W.I. Choi, S.-H. Jhi, K. Kim, Y.-H. Kim, Phys Rev B, 2010, **81**, 085441.

10 Z. Xin, W. Fengliang, K. Xiang-Peng, F. Ruiqi, L. Yingwei, J. Am. Chem. Soc., 2021, **143**, 16068-16077.

11 C.-L. Song, Q.T. He, Z. Zeng, J.-Y. Chen, T. Wen, Y.-X. Huang, L.-C. Zhuang, W. Yi, Y.-P. Cai, X.-J. Hong, Journal of Energy Chemistry, 2023, **79**, 505-514.

12 Z. Du, X. Chen, W. Hu, C. Chuang, S. Xie, A. Hu, W. Yan, X. Kong, X. Wu, H. Ji, L.-J. Wan, J. Am. Chem. Soc., 2019, **141**, 3977-3985,.

13 C. Zhao, G.L. Xu, Z. Yu, L. Zhang, I. Hwang, Y.X. Mo, Y. Ren, L. Cheng, C.J. Sun, Y. Ren, X. Zuo, J.T. Li, S.G. Sun, K. Amine, T. Zhao, Nat. Nanotechnol., 2021, **16**, 166-173.

14 S. Zhang, X. Ao, J. Huang, B. Wei, Y. Zhai, D. Zhai, W. Deng, C. Su, D. Wang, Y. Li, Nano Lett., 2021, **21**, 9691-9698.

15 Y. Li, Y. Zeng, Y. Chen, D. Luan, S. Gao, X.-W.D. Lou, Angew. Chem. Int. Ed., 2022, **61**, e202212680.

16 M. Cheng, Z. Youquan, F. Yiming, W. Ning, Z. Liangjun, L. Chaoping, C. Libao, L. Yanqing, J. Xiaobo, Y. Chenglin, W. Weifeng, Adv. Mater., 2021, **33**, e2100171.

17 Y. Li, G. Chen, J. Mou, Y. Liu, S. Xue, T. Tan, W. Zhong, Q. Deng, T. Li, J. Hu, C. Yang, K. Huang, M. Liu, Energy Storage Materials, 2020, **28**, 196-204.

18 Z. Liu, L. Zhou, Q. Ge, R. Chen, M. Ni, W. Utetiwabo, X. Zhang, W. Yang, ACS Appl. Mater. Interfaces, 2018, **10**, 19311-19317.

19 Y. Liu, Z. Wei, B. Zhong, H. Wang, L. Xia, T. Zhang, X. Duan, D. Jia, Y. Zhou, X.

Huang, Energy Storage Materials, 2021, **35**, 12-18.

20 J. Wang, L. Jia, J. Zhong, Q. Xiao, C. Wang, K. Zang, H. Liu, H. Zheng, J. Luo, J. Yang, H. Fan, W. Duan, Y. Wu, H. Lin, Y. Zhang, Energy Storage Materials, 2019, **18**, 246-252.

21 Y. Li, J. Wu, B. Zhang, W. Wang, G. Zhang, Z.W. Seh, N. Zhang, J. Sun, L. Huang, J. Jiang, J. Zhou, Y. Sun, Energy Storage Materials, 2020, **30**, 250-259.

22 L. Ma, J. Qian, Y. Li, Y. Cheng, S. Wang, Z. Wang, C. Peng, K. Wu, J. Xu, I. Manke, C. Yang, P. Adelhelm, R. Chen, Adv. Funct. Mater., 2022, **32**, 2208666.

23 L. Shen, Y. Song, J. Wang, C. Zhao, C. Bi, S. Sun, X. Zhang, B. Li, Q. Zhang, Small Structures, 2022, 2200205.